

Final Report

"Development of Graphene/SiC sensing platform for real-time detection of toxic heavy metals" (2016-2019, Agreement 16-541)

by Ivan Shtepliuk, Linköping University, Linköping, Sweden

Highlights

- High-quality monolayer epitaxial graphene on 4H-SiC has been grown by thermal decomposition of 4H-SiC in argon atmosphere.
- The high quality of grown samples was confirmed by Raman mapping analysis, optical reflectance mapping, atomic force microscopy, IV characterization, cyclic voltammetry and photoemission electron microscopy.
- The adsorption order of considered heavy metals is $Pb > Cd > Hg$.
- Enhanced stripping response of epitaxial graphene to Pb exposure was observed. A detection limit of 2 $\mu\text{g/L}$ has been achieved for Lead by using anodic stripping voltammetry.
- The adsorption energies of Cd and Hg are mainly governed by dispersion forces., while the adsorption energy of Pb is mainly determined by orbital interaction.
- Initial kinetics of selected heavy metals on epitaxial graphene is governed by three-dimensional diffusion-controlled instantaneous nucleation mechanism.
- During response-recovery test, the real-time detection of Pb by using graphene as a chemiresistor was possible as low as 120 nM. A detection limit is significantly smaller than the WHO permissible limit. The response and recovery time of the sensor are only 10 and 65 seconds, respectively.
- The conductometric response is driven by the formation of stable charge-transfer complexes, which cause the increase in hole conductivity of epitaxial graphene under Pb accumulation conditions.
- The proof of concept of the sensing platform which allowed continuous real time monitoring of toxic heavy metals was fully demonstrated and the features described in this project combined with the compactness of the system may allow its positioning directly along the water purification chains, thus facilitating sample study in real time.

Abstract

The *current project* was motivated by the urgent necessity to develop fast and real-time sensing platform based on epitaxial graphene on SiC for detection of toxic heavy metals (especially Cd, Hg and Pb) in water. This is since heavy metals belong to one of the most dangerous categories of persistent toxins with high bioaccumulation ability. In the frames of the project, *two different strategies* to design the sensors enabling real-time monitoring of heavy metals were implemented: (i) discriminative analysis by using Anodic Stripping Voltammetry (ASV) technique and (ii) fast Response-Recovery heavy metals detection based on monitoring of changes in graphene conductivity/resistance under metal accumulation conditions. Both methods exploit the epitaxial graphene on 4H-SiC as an active component of the detection system (working electrode or conductor/resistor). In this regard, the special focus was placed on a comprehensive study of the quality of this material. Homogeneous monolayer epitaxial graphene on silicon carbide was fabricated by thermal decomposition of a Si-face 4H-SiC wafer in argon atmosphere. The quality of the grown samples was then analysed by *I-V* characterization, micro-Raman spectroscopy and Photoemission electron microscopy. Extracted values of the Schottky barrier height

and the ideality factor are found to be 0.4879 ± 0.013 eV and 1.01803 ± 0.0049 , respectively, thereby implying uniformity of the Schottky barrier height over the whole area and a stable rectifying behaviour. Raman mapping analysis showed that the intensity over 121 spectra was uniform and only two main peaks (so-called *G* and *2D* modes) and the weak structured band related to the buffer layer (BL) were distinguishable. No Raman signal from the defect-related *D*-mode was detected, demonstrating the high crystalline quality of the epitaxial graphene before sensing tests. The homogeneity and revealed properties of grown epitaxial graphene samples are good prerequisites of designing highly sensitive portable devices for in situ monitoring of environmental pollutants.

By means of anodic stripping voltammetry and density functional theory (DFT) modelling, the adsorption behavior of three most toxic heavy metals (namely, Cadmium, Mercury and Lead) onto epitaxial graphene and revealed the relationship between stripping current density and adsorption energy. Electrochemical results indicate that epitaxial graphene exhibits different stripping behavior toward heavy metal species, enabling only detection of the Cd and Pb, while no stripping response for Hg was observed. To shed light on unsatisfactory stripping behavior of the Hg, more detailed analysis of the Hg-involved redox reactions was performed. Electrochemical tests by the probing of simultaneously present Cd and Pb in aqueous solution using the SWASV method were also conducted and showed that the epitaxial graphene response to Pb is much stronger due to the higher adsorption energy compared to Cd. It is verified that the epitaxial graphene exhibits quasi-reversible anode reactions in aqueous solutions, providing a well-defined redox peak for Pb species and good linearity over a concentration range from 1 nM to 1 μ M.

To perform Response-Recovery tests, 3D-printed microfluidic device exploiting epitaxial graphene as the conductor/chemiresistor was designed. It was revealed the excellent sensing activity towards Pb and Cd ions. Several concentrations of Pb^{2+} solutions, ranging from 125 nM to 500 μ M, were analyzed showing Langmuir correlation between signal and Pb^{2+} concentrations, good stability, and reproducibility over time. Upon the simultaneous presence of both metals, sensor response is dominated by Pb^{2+} rather than Cd^{2+} ions. A detection limit of 95 nM was extrapolated from the calibration curve, which is lower than the recommended safe limit (180 nM) provided by the World Health Organization (WHO) for lead levels in drinking water. The comprehensive theoretical computations allowed to understand the nature of the adsorption of heavy metals on epitaxial graphene under realistic models. Sensing mechanisms underlying the heavy metals detection were proposed.

The studies carried out during the project fulfilment (2016-2019) were then extended towards deep investigation of a nature of an interaction between other metals (Li, Ag and Cu, respectively) with epitaxial graphene.

During the project fulfilment period I published 22 peer-reviewed papers (with acknowledgements to The ÅForsk foundation), 2 popular science articles and gave 15 oral presentations.

Project Results

1. Growth and characterization of the monolayer epitaxial graphene on 4H-SiC

1.1. Growth of epitaxial graphene

Monolayer (1ML) epitaxial graphene films with high thickness uniformity were synthesised by the high-temperature thermal decomposition of the Si-face 4H-SiC substrate in argon atmosphere. It is important to note that such growth method allows to reach compromise between graphene quality and price comparing to other methods (the photo of Growth setup is shown in Figure 1). Our group led by Prof. Rositsa Yakimova exclusively developed growth protocols allowing to tune the operation conditions for large area graphene/SiC with given characteristics depending on the applications. For sensor processing there is a preference on large substrate size: 20x20 mm².

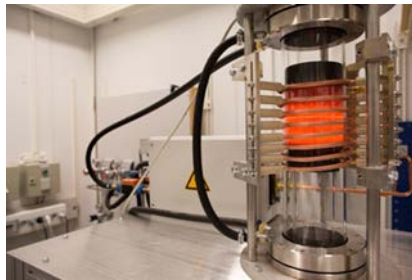


Figure 1. Experimental setup for graphene growth.

1.2. Optical reflectance mapping and atomic force microscopy (AFM)

The graphene layer on SiC template has terrace-stepped morphology, due to the unintentional misorientation of the SiC substrate and respectively a natural step bunching. As it was observed by AFM and reflectance mapping (Figure 2), the SiC surface is up to 93 % covered by monolayer of graphene. The overgrowth of bilayer is rarely observed.

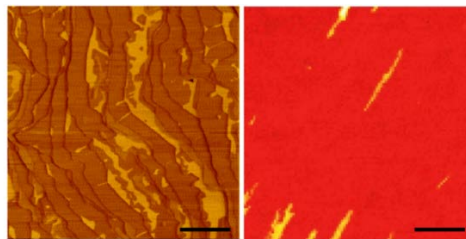


Figure 2. (left panel) AFM image and (right panel) optical reflectance map of typical monolayer epitaxial graphene sample before sensing tests. Scale bars on both images are 2 μm .

1.3. Raman mapping analysis

The vibrational properties of as-grown samples were investigated by Raman spectroscopy with the aim to address the question on stability of the epitaxial graphene as chemiresistor and/or working electrode. Indeed, from the practical point of view it is very important to utilize the chemiresistor and/or working electrode having understandable and reproducible properties. In this context, Raman measurements can be used to give quick feedback on the quality of epitaxial graphene samples, including defect density, number of graphene sublayers, homogeneity and so on. To test whether the epitaxial graphene is uniform

enough to be used as chemiresistor and/or working electrode, we collected a set of Raman spectra on a square map ($3\ \mu\text{m} \times 3\ \mu\text{m}$, $0.3\ \mu\text{m}$ pitch). Figure 3 (left panel) exhibits the two-dimensional color-coded plots of the set of 121 Raman spectra (see also the corresponding zoomed spectral regions in the middle and right panels). It is clearly seen that the intensity over 121 spectra is uniform and only two main peaks (so called G and $2D$ modes) and the weak structured band related to the buffer layer (BL) are distinguishable. We do not detect any Raman signal from the defect-related D mode, demonstrating the high crystalline quality of the epitaxial graphene.

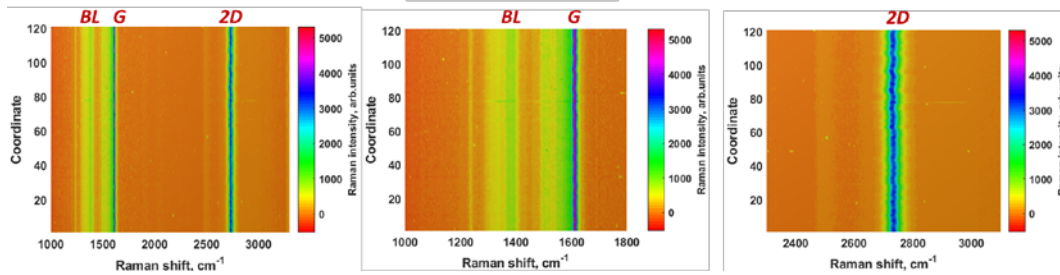


Figure 3. Two-dimensional contour plots of Raman spectra of as-grown epitaxial graphene conveying both the intensity and spectral uniformity of the predominant vibrational G and $2D$ modes. The whole Raman fingerprint of the epitaxial graphene and the regions zooming in the vicinity of the G and $2D$ peaks are depicted in the three panels from left to right, respectively.

Simple statistical analysis on the set of 121 Raman spectra was used to estimate the uniformity of the Raman scattering intensity. We calculated the relative standard deviation (RSD) of intensities of the characteristic G and $2D$ Raman modes. RSD values for these peaks are found to be 3.2% and 3.7%, respectively, indicating that the as-grown epitaxial graphene possesses excellent Raman scattering uniformity. Taking the aforementioned into account, we anticipate that sensing performance of epitaxial graphene will be determined by the direct interaction between analyst (heavy metals in our case) and defect-free sp^2 conjugated graphene domains.

1.4. Current-voltage characterization

I - V characteristics of the monolayer graphene/SiC vertical devices display a rectifying behavior (Figure 4). The depicted curves correspond to different measurements of the same device with six Pd contacts.

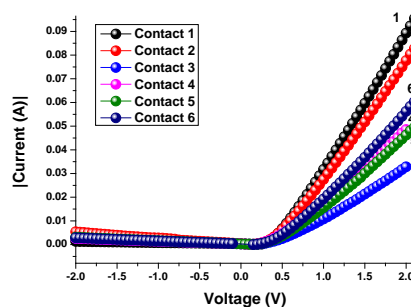


Figure 4. Current-voltage characteristics of the vertical graphene/4H-SiC device. The vertical y-axis indicates the absolute values of current. Palladium contacts (1-6) are positioned at the different places of the graphene surface.

In order to get information about statistical distribution of the Schottky barrier height (SBH) and ideality factor we carried out the several additional measurements for each palladium point contact. Obtained results suggest that the rectifying behavior of the graphene/SiC diode is very stable. According to the statistical distributions, the determined SBHs range from 466 meV to 503 meV for graphene/SiC junction, whereas the ideality factor ranges from 1.0115 to 1.026. The standard deviations yield 0.013 eV and 0.0049 for both parameters, respectively. The mean values of SBH and ideality factor of the Schottky diode are 0.4879 eV and 1.01803, respectively. The extracted value of the Schottky barrier height is in good agreement with the theoretical value 0.5 eV. Furthermore, comparing to literature data our samples are characterized by much smaller value of the standard deviation for the Schottky barrier height. It can be explained by assuming the presence of the high thickness homogeneity (99% according to reflectance mapping) and barrier height uniformity. The derived values of the ideality factor of a diode junction suggests that the diode behaves itself closely to the ideal case, thereby implying the minimized role of some undesirable phenomena, such as presence of interface states, generation-recombination, tunneling and even spatial inhomogeneity. High quality of the graphene surface and low density of defects promote also the low series resistance of the diode and reduced leakage current. The average values of the series resistance and saturation current were found to be equal to 34 Ω and $9.577 \cdot 10^{-4}$ A, respectively.

1.5. Photoemission electron microscopy (PEEM)

The work function mapping by PEEM technique has been also performed to get more information on quality of the as-grown samples (Figure 5). The figure demonstrates the calibrated work function map of the mono-layer graphene, which exposes some local variations in the work function, due to substrate charge inhomogeneities and bilayer inclusions.

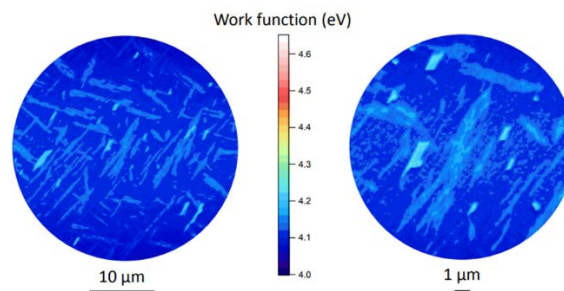


Figure 5. Work function maps for typical monolayer epitaxial graphene sample before sensing tests.

1.6. Cycling voltammetry

Understanding the basic electrochemical behaviour of epitaxial graphene is the prerequisite to develop the working electrode material with desired properties for the construction of the effective electrochemical cell for heavy metals detection. Starting with cyclic voltammetry measurements in 0.1 M acetate buffer solution, we revealed a very small dark current (absence of any faradaic processes) in the potential region between -0.6 and 0 V (Figure 6). This implies that there are no redox species

(nonorganic and/or organic substances) in electrolyte, which could show the oxidation activity. Moving towards more negative potentials, the current starts to increase due to the reduction of water. In fact, the electrolysis of water is strongly undesirable phenomenon in the light of the metal sensing, because it causes the degradation of the working electrode and gas bubbling at the surface of the electrode. Due to this reason the potential window for redox reactions involving heavy metals is usually shortened and thus electrochemical performance of working electrode towards identification of the metal is not satisfactory. Despite the hydrogen evolution reaction (HER) starting at approximately -0.6 V, the potential window of epitaxial graphene for recognition of heavy metals species is found to be wide enough to prevent the overlapping heavy metals stripping peaks and water reduction region.

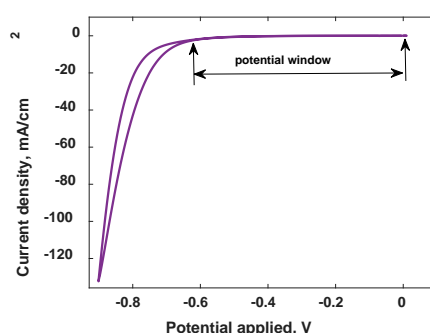


Figure 6. Cyclic voltammetry of epitaxial graphene working electrode in the acetate buffer solution (0.1 M, pH 4.65) with Ag/AgCl reference electrode and Pt wire as counter electrode.

2. Electrochemical detection of heavy metals by using ASV technique

2.1 Construction of the Electrochemical cell

Computer-controlled potentiostat (Autolab, EcoChemie, Netherlands) was used in all room-temperature electrochemical measurements. The laboratory-made electrochemical cell of o-ring type (Figure 7) was coupled with working electrode (Gr/SiC anode), reference electrode (Ag/AgCl) and counter electrode (platinum wire).

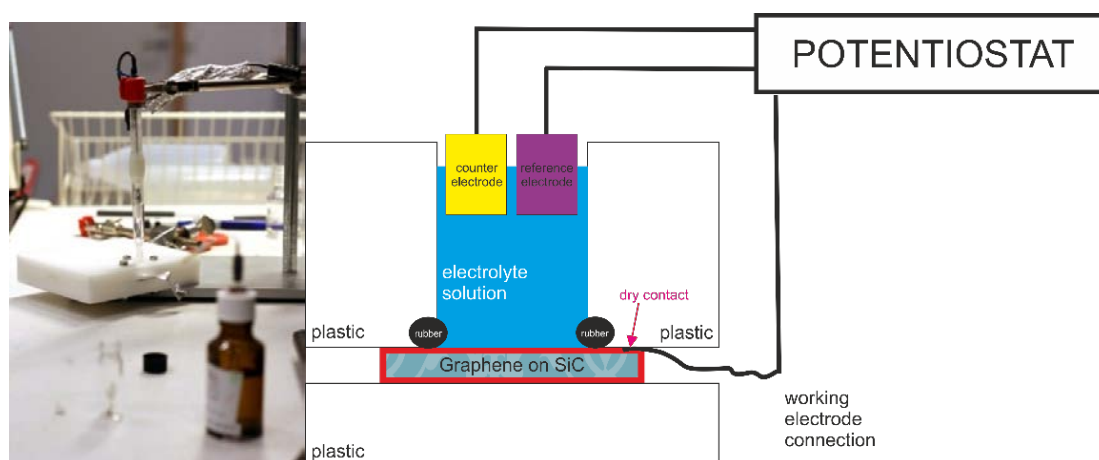


Figure 7. (left panel) A photo of the three-electrode electrochemical cell and (right panel) a schematic illustration of the electrochemical cell.

2.2 ASV measurements

Since each of heavy metals has the specific redox potential and interacts with graphene in unique manner, the different stripping current peaks are expected. The corresponding two-dimensional contour plots of anodic stripping current conveying both the current density and HMs concentrations are presented in Figure 8. It is clearly seen that no stripping response was observed in the case of Mercury. It can be explained by the very small intrinsic adsorption energy of Hg on the surface of the graphene electrode, which is not enough to accumulate metal species required for generating the stripping current. A close look at contour plots describing the response of the graphene to Cd and Pb confirms that SiC-supported monolayer graphene provides single, well-defined stripping peak currents at the certain potentials, which are proportional to the concentration of Cd^{2+} and Pb^{2+} , respectively. Visual analysis of the maps suggests that the graphene is more sensitive to Pb than to Cd, which is evidenced by an earlier appearance of the signal during Pb-involved reduction-oxidation processes at the graphene surface. In other words, due to faster electrode reactions, the striping-peak current starts to appear at smaller Pb concentrations. To obtain quantitative information about sensitivity of graphene to different metals, the dependences of the stripping-peak current density on the concentrations of the Cd and Pb ions are investigated (see Fig 9a and b, respectively). It is obvious that both dependences exhibited a linear relationship. For the Cd ion (Fig. 9(a)), the linear-regression equation is calibrated as $I_{\text{Cd}}(\text{mA}\cdot\text{cm}^{-2}) = 8.6 \times 10^4 \cdot [\text{Cd}(\text{mol/L})] + 0.066$, with a correlation coefficient of 0.9951 and a sensitivity of $8.6 \times 10^4 \text{ mA}\cdot\text{cm}^{-2} \cdot \text{mol}^{-1}\cdot\text{L}$. While the correlation equation for Lead is $I_{\text{Pb}}(\text{mA}\cdot\text{cm}^{-2}) = 2.3 \times 10^6 \cdot [\text{Pb}(\text{mol/L})] + 0.9$ with a correlation coefficient of 0.9945 and sensitivity of $2.3 \times 10^6 \text{ mA}\cdot\text{cm}^{-2} \cdot \text{mol}^{-1}\cdot\text{L}$ (Fig. 9(b)).

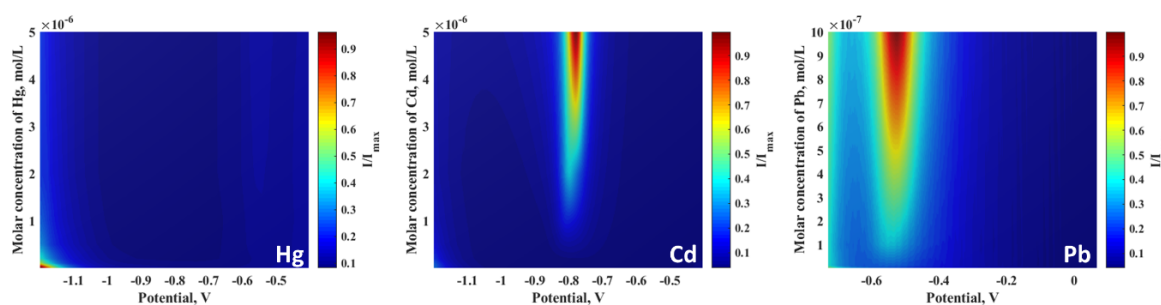


Figure 8: Two-dimensional contour plots showing the current density as a function of potential and metal concentrations for epitaxial graphene (epitaxial graphene on Si-face 4H-SiC) electrode after exposure to different heavy metals: Hg^{2+} , Cd^{2+} and Pb^{2+} (see from the left to the right). The current maps were constructed based on ASV measurements. Brighter regions correspond to a higher current density. The values of anodic stripping current density are normalized to the maximum value of current density for each case considered.

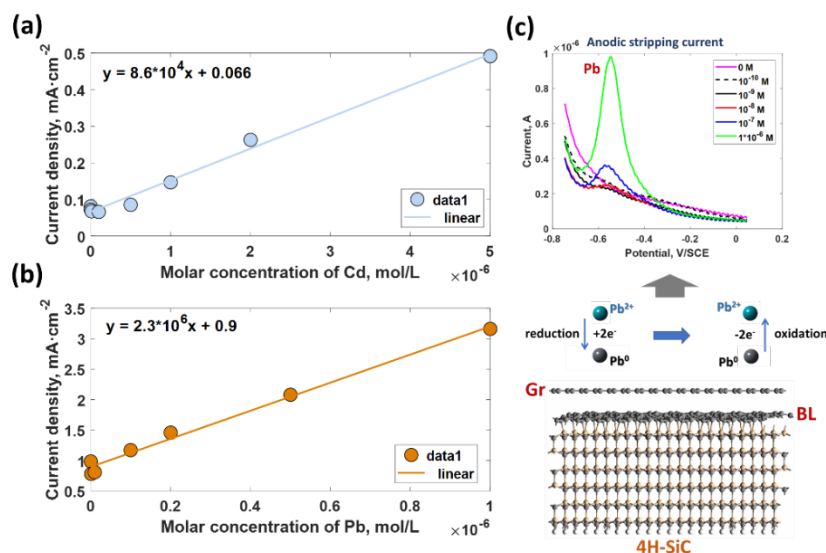


Figure 9: Calibration curves for (a) Cd²⁺ and (b) Pb²⁺ and (c) schematic of the sensing mechanism for the detection of Pb²⁺ ions

2.3 Sensing mechanisms

The sensing mechanism in the case of the electrochemical detection is governed by the interaction between elemental (reduced) metal species and graphene (Fig. 9c). In fact, divalent metal ions (M²⁺) are initially reduced to neutral metal species (M⁰) at a specific potential. Immediately after, anodic stripping current related to their re-oxidation identifies the amount of metal species adsorbed onto the electrode surface. The stronger adsorption ability of metal, the more intensive current peak. The enhanced sensitivity of graphene to Pb species and observed limit of detection correspond well to modern WHO requirements for critical concentrations of Pb in potable water. Despite the existing HMs sensors demonstrate even more superior sensitivity, in most cases a synthesis of sensitive materials is multistage technological process, which demands functionalization and/or immobilization steps. In this regard, graphene itself exhibits strong ability to Pb binding (Figure 10), thereby offering some advantages over other sensing platforms.

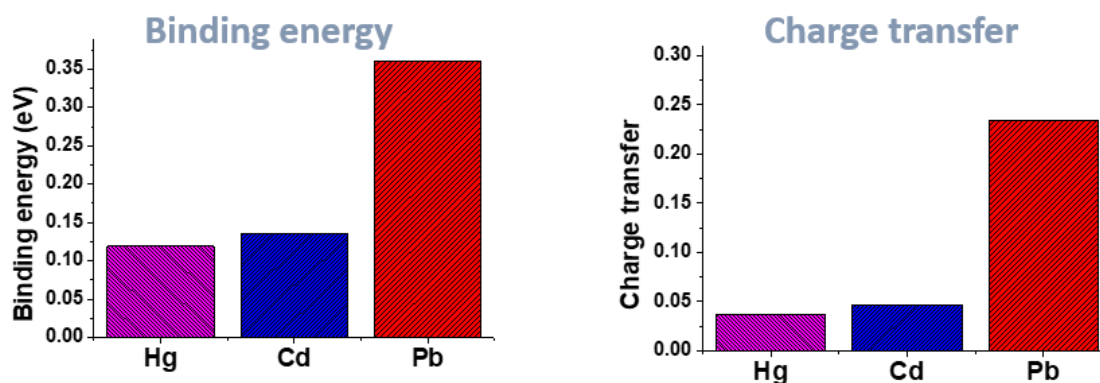


Figure 10. Histograms of binding energy of heavy metals and charge transfer between heavy metals and graphene, respectively.

The selective response of graphene is also predicted by DFT by comparing the binding strengths for considered metals (Figure 10). The supercell calculations find minimal charge transfer between the physisorbed cadmium and mercury adatoms and the graphene sheet, which is significantly smaller than charge transfer between Pb atom and the graphene sheet (Figure 10). The effects of this charge transfer can be seen in the shift of the graphene Dirac cone towards higher binding energies after Pb adsorption (Figure 11). While for Cd and Hg, the Dirac point remains at the Fermi level, when Pb is adsorbed on graphene the Dirac point is shifted to 0.48 eV below the Fermi level, due to the strong n-doping from the adsorbant. It is apparent that the adsorption ability of epitaxial graphene toward Pb species is expected to be much stronger than those toward other HMs under accumulation conditions.

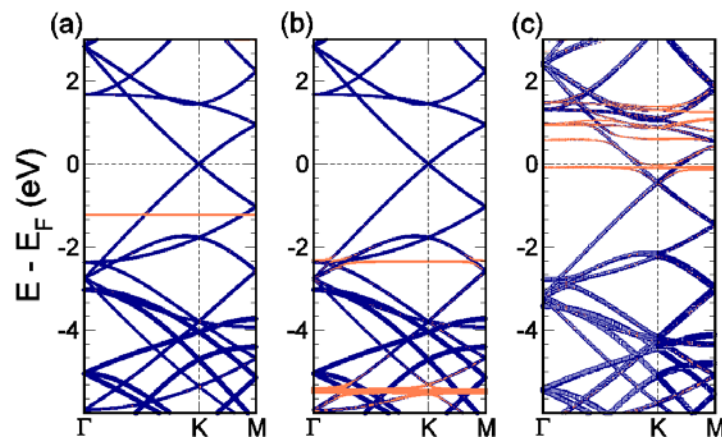


Figure 10. Band structure of (a) Cd, (b) Hg and (c) Pb atoms adsorbed on a 4 x 4 graphene supercell.

The purple lines denote those bands with a large graphene character, while the orange lines have a higher character from the metal adatom. This band character was determined by projecting onto the atomic orbitals of the respective atoms. The band thickness represents the magnitude of the overlap.

By using DFT calculations, we revealed that the cadmium and mercury adatoms can diffuse freely across the graphene surface, while the Pb atom must overcome high energy barrier exceeding 0.1 eV (Figure 11). It was also found that under conditions of the simultaneous presence of both cadmium and Lead, Lead predominantly tends to occupy the available electrochemical reactive sites the at graphene surface. While Cd species are less involved in stripping process within investigated concentration range.

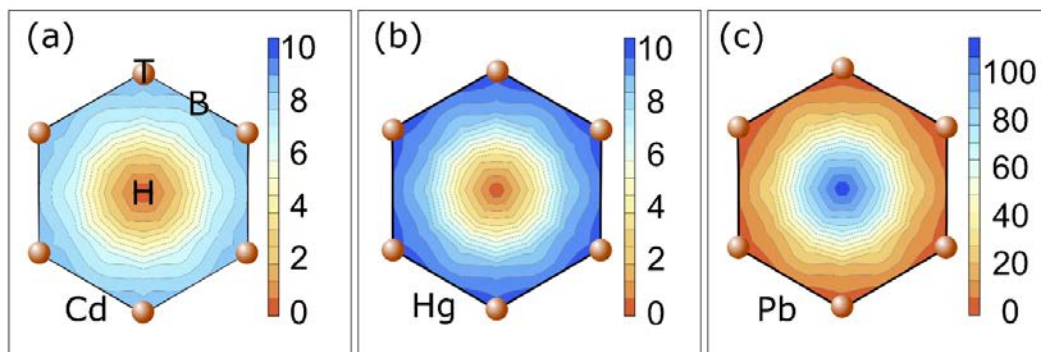


Figure 11. Total energy (in meV) as a function the (a) Cd, (b) Hg, and (c) Pb adatom position on a graphene hexagon, calculated for a 4 x 4 supercell. In all cases, the minimum total energy is set to 0eV. Note the change in scale for (c).

2.4. Simultaneous detection of Pb and Cd

To test the cross-sensitivity of the epitaxial graphene, we mixed both solutions containing Lead and Cadmium ions. The results are shown in Figure 12. Well-defined intensive stripping current peak (with a current density proportional to the concentration of the metal ions) is observed at approximately -0.43 V only for Lead case. This peak starts to appear at the concentration of $5 \cdot 10^{-7}$ M Pb^{2+} . In contrast to detection of Pb ions, the sensitivity of the epitaxial graphene towards Cd ions is much worse. Initially, electrochemical measurements of the graphene response to exposure of both Cadmium and Lead ions were performed at the same metal concentrations. Since stripping current peak is found to be very faint even at high Cd^{2+} concentrations, we then changed measurement conditions. After reaching the equilibrium concentration of $1.2 \cdot 10^{-6}$ M for both metals in solution, we then continued to increase only Cd^{2+} concentration, but maintaining the Pb concentrations at the same level. Under accumulation conditions, the Cd-related peak was detected only at Cadmium concentration of $1 \cdot 10^{-4}$ M. Immediately after, we noticed the enhancement of this peak at higher concentrations of metals. Such a difference in metals behaviour can be ascribed to the unique interaction nature and preference for Pb adsorption compared to Cd. It is likely under conditions of the simultaneous presence of both metals, Lead predominantly tends to occupy the available electrochemical reactive sites the at graphene surface. While Cd species are not involved in stripping process within corresponding concentration range. It can be explained by the very small intrinsic adsorption energy of Cd on the surface of the graphene electrode, which is not enough to accumulate metal species required for generating the stripping current.

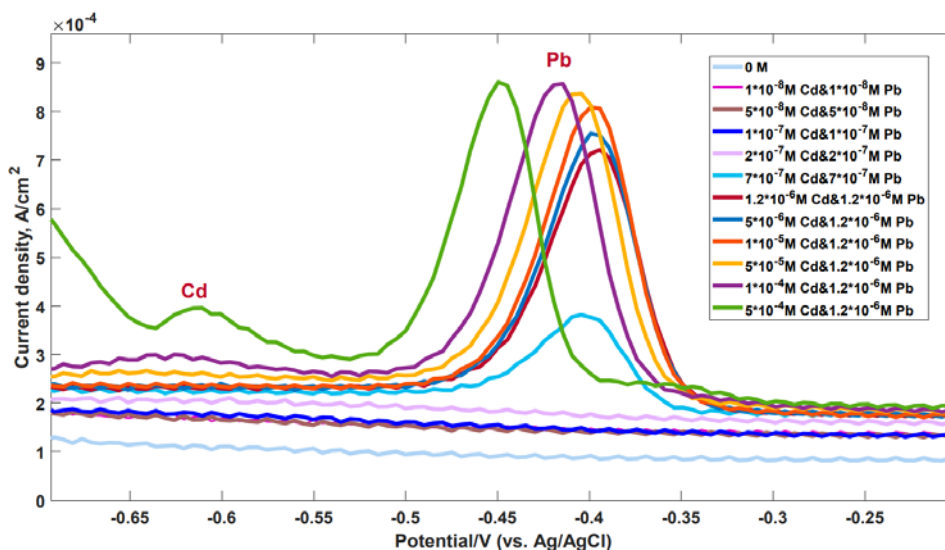


Figure 12. SWASV electrochemical response of the graphene electrode for the simultaneous analysis of Cd^{2+} and Pb^{2+} .

To explain the experimental results, we simulate the solvent-mediated interaction between elemental heavy metals and graphene. From analysis of electron localization function and localized orbital locator images (Figure 13), it is clearly seen that there is no electron localization overlap between Cd and

graphene, while the electrons are shared between Pb and carbon atoms pointing out a larger interaction strength.

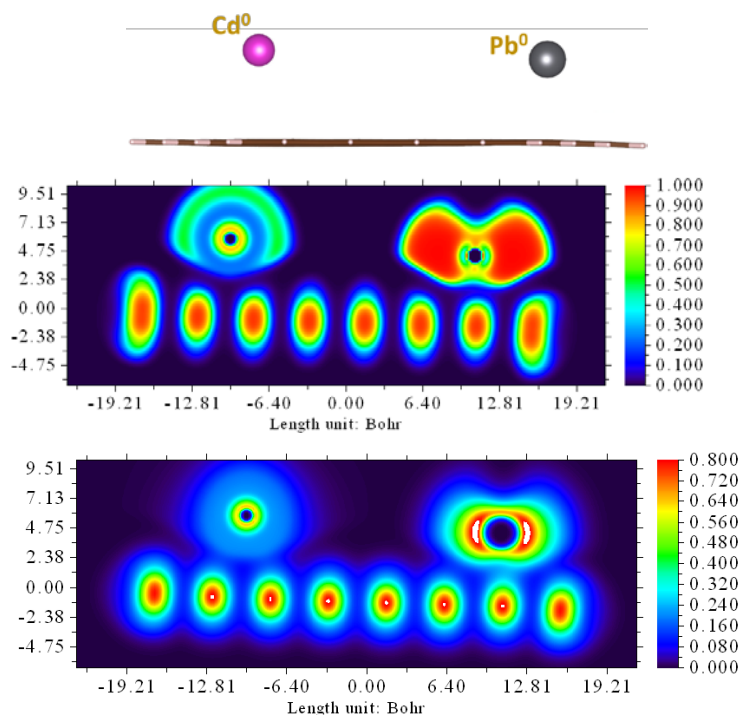


Figure 13. (from the top to the bottom) Side view of the relaxed adsorption configurations of simultaneous adsorption of Cd⁰ and Pb⁰ metal adatoms on graphene surface and corresponding contour plots of the electron localization function (ELF) and color-filled maps of localized orbital locator (LOL).

3. Conductometric detection of heavy metals by performing Response-Recovery tests

3.1. Construction of detection system

The sensor used for this application exhibits a physical size of 7 mm × 7 mm, and it was fabricated by deposition of four electrodes on top of the graphene surface as reported in Fig. 14(a). The electrodes were realized by sputter deposition of 2 nm of titanium and 200 nm of gold sequentially, and they are 1 mm in diameter. The sensor is fixed on a matrix board and its electrodes are connected to four electrical wires (a, b, c, d), welded on the bottom of the board, using gold bonding wires glued by a conductive silver paste (Epotek H20E), as illustrated in Fig. 14(a). It is biased through a 2601 A Keithley Source Meter, which also acquires the output signal. A 3D printed fluidic cell was designed and fabricated for the purpose, and fixed on top of the sensor. Thanks to the pressure applied by four screws placed in the corners of the chip, the chamber is perfectly sealed to the sensor. The real-time monitoring of the heavy metals is performed using two NE-1010 Higher Pressure Programmable Single Syringe Pumps which inject the buffer solution (deionized water – dH₂O) and analyte (heavy metals) in a microfluidic chip where the mixing takes place, before reaching the fluidic cell where the detection occurs (Fig. 14b). The measurements were performed by biasing the sensor with a 2601 A Keithley Source Meter between two corner contacts, using a software which allowed control of the bias voltage (fixed at 3 V) and the

measurement conditions (time of measurement), and acquired the output signal automatically. The signals were analyzed offline by a routine developed in Matlab and Origin. The fluidic chips, the flow cell and the mixing chip, were designed using CAD software (Autodesk Inventor Fusion, Autodesk Inc.). Both chips exhibit open channels, allowing easy access for functionalization, and the sub-micrometric surface finishing enables sealing with regular transparent adhesive tape. They were fabricated through a Form 1+ [21] 3D printer, using a proprietary resin Clear Type 02, which includes different proportions of modified acrylate and acrylate oligomer, epoxy monomer, acrylate monomer, photo initiator and additives as the principal components. After printing, both chips were sonicated in ethanol for a few minutes and the open side of the channels was sealed by transparent adhesive tape. The microfluidic chip dedicated to the mixing between the buffer solution and analyte includes a 3D bulk serpentine mixing, and two inlet and an outlet port with an internal radius of 500 μm . The mixed solution is then injected through the inlet port of the main microfluidic chip to the flow cell that exhibits a volume of $\sim 7 \mu\text{l}$ where the solution reacts with the sensitive surface. After the measurements, the solution goes through a returning channel connected to a beaker used as waste reservoir. The inlet and the outlet ports of the main chip both exhibit an internal radius of 500 μm .

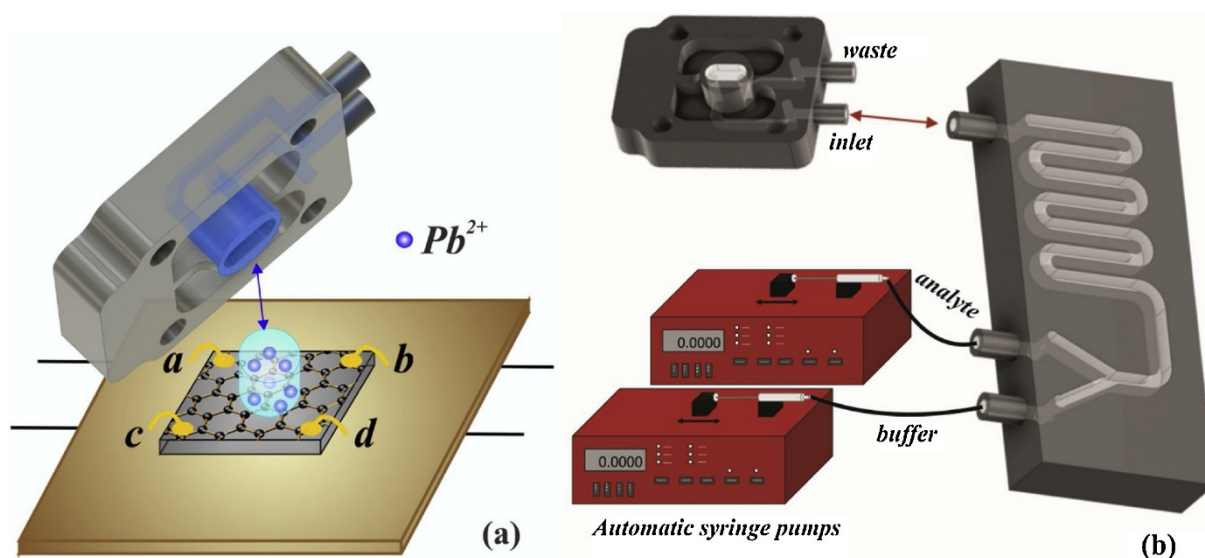


Figure 14. Schematic of board mounting process (a) and experimental setup (b).

3.2. Resistance-time measurements

The dynamic performance of the sensing platform based on epitaxial graphene (EG/SiC) for liquid-phase detection of HMs was evaluated by measuring different concentrations of Pb^{2+} solutions, ranging from 125 nM to 500 μM . Evaluation of the sensing system performance was carried out using the setup described above, and reactants were injected into the microfluidic chip at a fixed flow rate of 19.2 ml/h using two programmable syringe pumps. The calibration curve presented in Fig. 15 was obtained by

analyzing the sensor performance in response to a full set of Pb^{2+} concentrations (0.125, 0.25, 0.5, 5, 50, 200, 350, 500 μM). The values and the errors reported in the calibration curve are the averages of several repetitions of the signals recorded for each Pb concentration after subtraction of the reference signal, on three different measurements.

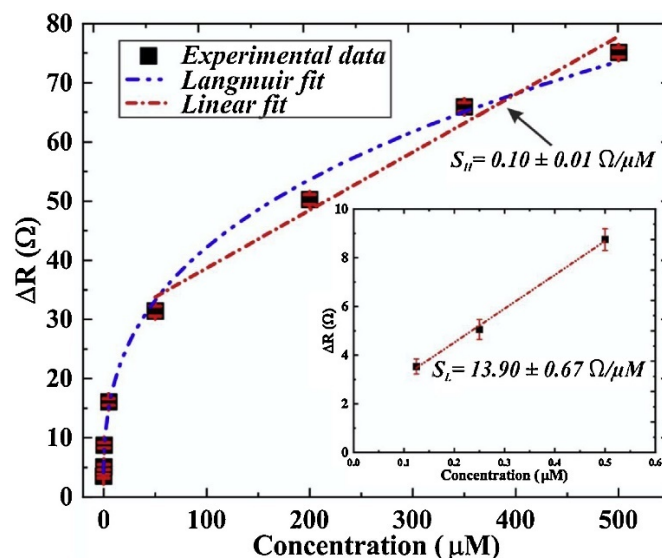


Figure 15. Calibration curve showing the dependence of the differential resistance on the Pb concentration. The inset zooms into the initial part of the curve at low Pb concentrations. The red straight lines are linear fits to different parts of the curve, illustrating the different sensitivity at low and high concentrations.

The sensor was able to detect low traces of Pb^{2+} ions (125 nM), which is lower than the recommended limit for Pb contamination in drinking water provided by WHO, set at 180 nM. Furthermore, the system exhibited a signal-to-noise-ratio (SNR) of 7.1 dB at that concentration of Pb^{2+} ions. We demonstrate that solvent-mediated interaction of Pb^{2+} ions with EG enhances its conductivity. In accordance with Langmuir's law, increasing the Pb^{2+} concentration leads to increase of differential resistance value, since more divalent ions are adsorbed on EG surface. Even though Langmuir relation is observed, it is possible to extract two different sensitivities for low and high concentrations of Pb^{2+} from the calibration curve. Indeed, sensitivities of $13.90 \text{ } \Omega/\mu\text{M}$ and $0.10 \text{ } \Omega/\mu\text{M}$ were obtained for low (0.125–5 μM) and high (50–500 μM) concentration ranges of Pb, respectively, approximating linear sensitivities in these limited ranges. This means that the system is more sensitive to low concentrations of Pb, and it confirms the results obtained from the DFT calculations. Indeed, increasing the concentration of Pb^{2+} ions decreases the per-ion energy transfer between Pb^{2+} and graphene. This result enhances the extreme sensitivity of graphene towards low traces of lead ions. Considering the sensitivity calculated for low Pb^{2+} concentrations, we calculated a theoretical detection limit (LoD) of 95 nM.

Moreover, we demonstrated the system potential for continuous-flow monitoring of HMs by injecting the reactants automatically into the microfluidic chip for detection of four different concentration of lead ions (0.5, 5, 50, and 500 μM). Deionized water was also used as buffer solution to

wash the channels between sequential analyte exposures. The signal of the time-resistance response is reported in Fig. 16.

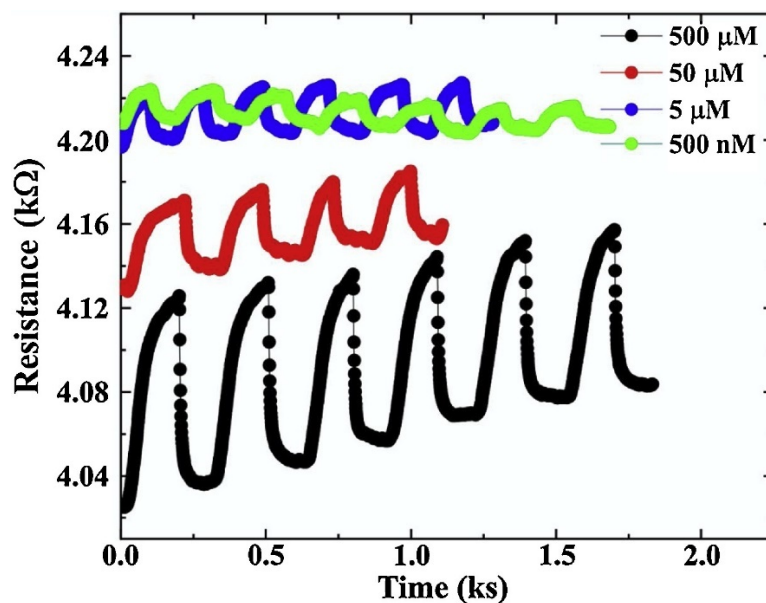


Figure 16. Sensor signal (resistance) versus time for Pb^{2+} concentration of: 0.5 (green line), 5 (blue line), 50 (red line), 500 μM (black line).

Data show the signals were stable and reproducible over time (few hours), but only few cycles were here reported. However, the increasing of Pb baseline, that we sometimes observe, could be due to a small change in the solution/ambient temperature. The filling time constant (τ_f) is 10.8 ± 0.6 s, while the emptying time constant (τ_r) is 65.4 ± 1.69 s for all repetitions at the highest concentration, as obtained from data fitting. Rise and fall time values were calculated as three times the corresponding characteristic time (τ_r and τ_f , respectively), hence we obtained $t_r = 34.4 \pm 1.8$ s and $t_f = 196.2 \pm 5.1$ s. The system described in this work has shown new interesting features in the field of rapid and accurate detection of heavy metals in solutions. Moreover, the sensor used in this study was used for more than one year in different operating conditions (analyte concentrations, different species, etc) and it did not shows any degradation in performance. Extreme sensitivity has been proved, and considerations concerning selectivity are still in progress.

Characterization of the system was also performed using drinking water in which other ions are present in addition to lead, and comparing the performance obtained for the highest concentration of lead (500 μM) we obtained a ΔR reduction of almost 35% (Fig. 17). For this reason, increasing the proportion of the device area exposed to the analyte is needed to improve the sensitivity, and the functionalization of the graphene surface or filtering steps and recognition process of the species (peptides, antigen-antibody, etc), which could be performed outside the sensing system, are needed to improve the selectivity of the proposed platform for real field applications. In addition, multivariate statistics analysis could be performed in order to distinguish different species only considering response time and signal shapes.

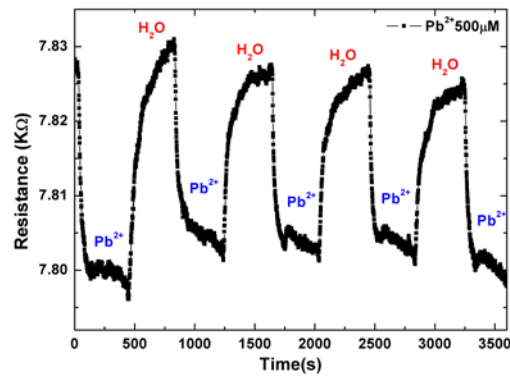


Figure 17. Sensor signal (resistance) versus time for Pb^{2+} concentration of $500 \mu\text{M}$ dissolved in drinking water.

The epitaxial response to lead was compared to the one obtained measuring the same molar concentration ($500 \mu\text{M}$) of Cadmium ions (Cd^{2+}), and reported in Figure 18a. It was demonstrated that Cadmium exhibits a lower affinity to graphene, compared to lead, and it is visible from different features like amplitude of the signal response and time response. Concerning the amplitude, in the same operating conditions in terms of molar concentrations of analyte, Cadmium exhibits a response DR of 67Ω compared to 76Ω provided by Lead (Figure 18a). Moreover, Cadmium needs more time to be adsorbed by the graphene surface, compared to Lead, due to the less affinity, and it means that the time response of Cadmium results much slower (around 41s) than the one corresponding to Lead (around 11s). Comparing the shape of the two signals, we observed that the signal provided by Cadmium exhibits a shoulder at about half of its total amplitude, confirming the different type of interaction with the graphene surface. To test the cross-sensitivity of the sensor system we mixed both solutions containing Lead and Cadmium ions with a concentration of $500 \mu\text{M}$ for each, and we observed that the resulting signal exhibits roughly the same amplitude of the Lead response, an intermediate time response (around 33s) and a little shoulder due to the presence of Cd (Figure 18b). Only at high concentration levels of analyte was possible to detect the presence of Cadmium, since the EG response to Lead is much stronger due to the higher affinity.

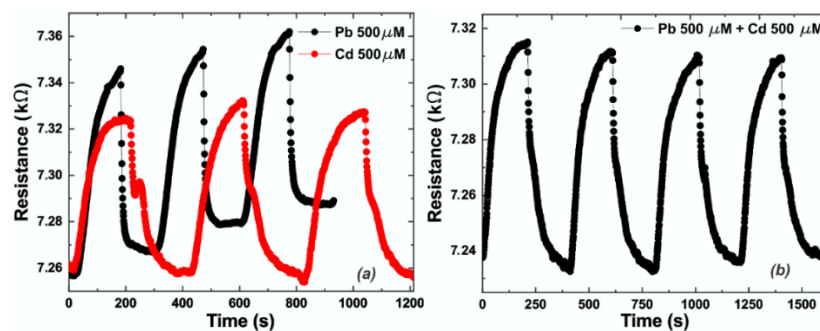


Figure 18. (a) Comparison between EG responses (resistance) to a concentration of $500 \mu\text{M}$ of Pb^{2+} (black line) and Cd^{2+} (red line) versus time; (b) EG response to a complex sample in which both solutions of Pb^{2+} and Cd^{2+} with a concentration of $500 \mu\text{M}$ were mixed.

3.3. Sensing mechanisms

Since the experimental data indicate a change in the graphene conductivity after interaction with Pb^{2+} ions, it is important to understand the nature of such changes. It is obvious that the change in the electronic properties of the system is originating from the charge transfer between the adsorbates and graphene. Our theoretical studies indicate that Pb^{2+} ions after adsorption on graphene act as electron-acceptors, with a preferential charge transfer from graphene to divalent ions (Fig. 19). To shed more light on the bonding of Pb^{2+} ions to graphene we calculated localized orbital locators (LOL) for all considered adsorption configurations. Figs. 19e and 19f exhibit two representative LOL maps, demonstrating the bonding electron density localization between Pb ions and carbon atoms. It is clearly seen that strong covalent C-C bonds are only depicted in yellow and red regains, while pale green regains suggest weaker bonds between Pb ions and carbon atoms. It is more likely that the Pb-C bonding is formed through the interaction between p_z orbital of C (each carbon atom contributes one delocalized electron) and valence orbital of metal.

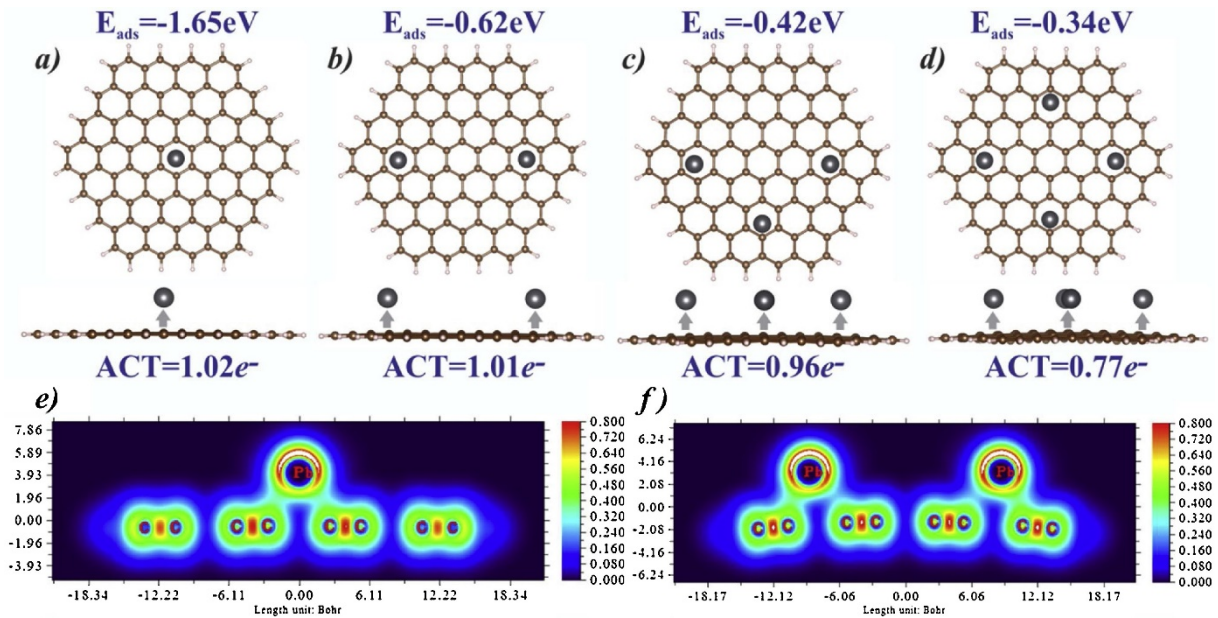


Figure. 19. (a–d) The optimized structures of divalent lead ions adsorbed on the graphene surface. The average values of charge transferred from graphene to one Pb ion (ACT) and adsorption energy per ion (E_{ads}) are also reported. The ACT and adsorption energy decrease with increasing the number of Pb ions. This is due to dipole-dipole interaction, which lowers the adsorption energy of the metal ions on the graphene surface. Localized orbital locator (LOL) maps are also reported for graphene interacted with one ion (e) and (f) four ions. Localized electrons are shown by yellow-red colors. The pale green represents delocalized electrons, while the electron depletion regions are depicted by the blue circles.

The transport of charge carriers through graphene will be determined by the non-equilibrium hole concentration (hole conductivity regime). The presence of a solvent (in this case an aqueous solution) will attenuate the cation- π interaction, without affecting the direction of the charge transfer. It is worth noting that we neglect the influence of the silicon carbide substrate. Such a simplification is justified by

the fact that the substrate can only affect the relative magnitude of the charge transfer, without affecting the direction of charge-transfer reactions. Indeed, since the water molecules on graphene are considered as electron-accepting (*p*-type) dopants, then conductivity measurements for *n*-type graphene on 4H-SiC (the *n*-type doping is originating from substrate) interacting with dipole moments of water molecules will be performed in the hole conductivity mode. In other words, epitaxial graphene that originally exhibits *n*-type behavior in vacuum conditions readily changes to *p*-type under water exposure. Therefore, a presence of charged Pb species in water electrolyte will influence the *p*-type conductivity of graphene. Increasing the concentration of Pb ions, total charge transferred from graphene to Pb^{2+} also increases, thereby leading to lowering of the Fermi level and an increase in hole conductivity. However, increasing the concentration of Pb^{2+} ions decreases the per-ion adsorption energy (E_{ads}) of Pb^{2+} from -1.65 eV (for 1 ion) to -0.34 eV (for 4 ions) (Fig. 19), which implies that sensitivity at small and high concentrations of Pb will be different. We also calculated the average values of charge transferred from graphene to one Pb ion (ACT), which, like the adsorption energy, decrease with increasing the number of Pb ions. This is due to dipole-dipole interaction, which lowers the adsorption energy of the metal ions on the graphene surface.

The DFT results indicate that the hollow site (center of the hexagonal ring) is the most favorable site for Pb^{2+} adsorption, with the per-ion adsorption energy of about -0.34 eV (at the largest concentration of the Pb^{2+} , i.e. four ions in our case). This means that the sensing mechanism of the Pb ions in pure aqueous solutions is governed by chemisorption processes with fast charge-transfer reactions near the hollow sites of the graphene. Knowing the adsorption characteristics enables not only to understand the sensing mechanism, but also permits to predict the recovery time of graphene-based sensor. It is known that the recovery time increases with the increasing adsorption energy. Therefore, the faster recovery time of epitaxial graphene sensor is expected at higher Pb concentrations, when the interaction between Pb ions and graphene is weakened. It was found that the major difference between Cd^{2+} and Pb^{2+} adsorption can be understood in terms of the charge-transfer reactions and subsequent solvent-mediated stabilization of the carbon-metal bonding. It was found that the adsorption of electron-accepting Pb ions is governed by orbital interaction, while Cd^{2+} behavior on graphene is predominantly regulated by long-range dispersion forces.

4. Understanding of metals kinetics at epitaxial graphene

4.1. Pb kinetics

To elucidate the Pb kinetics on the epitaxial graphene surface, the current transients were recorded as a response of applied potential pulses of different amplitudes preconditioned at the region of the complete Lead ionization (-0.2 V). The evolution of the current transient shapes with increasing the cathodic potential pulse amplitude (Fig. 20) shows a transition from the nucleation rate control to the reactant diffusion control observed on shorter and longer elapsed times, respectively. The appearance of Pb nuclei accompanied with the current increase due to the nuclei growth is visible at the short-elapsed times. The longer times are featured with the overlapping of convergent diffusion profiles of Pb ions yielding the suppression of growth rate and decrease of recorded currents. The increase of cathodic

polarization as the intensification of the deposition leads to the higher current densities (I_{\max}), while and shorter times until the control transition t_{\max} (Fig. 21a).

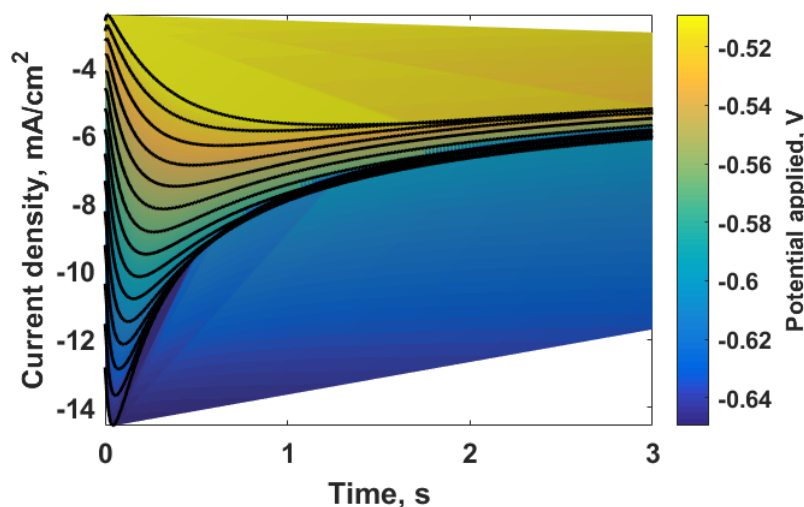
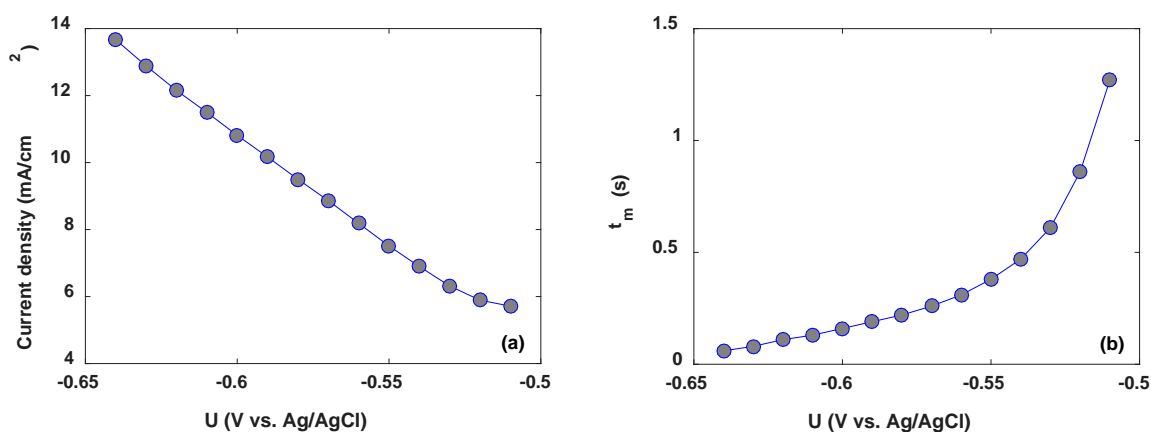


Figure 20. The evolution of current transients recorded on Gr/SiC at the cathodic potential pulses of different amplitudes (from -0.2 V to -0.64 V; 0.1mM $\text{Pb}(\text{NO}_3)_2$ in 0.1 M HClO_4).

When the deposition potential is shifted towards more negative potentials, the maximum time, corresponding to maximum current, tends to become shorter (Fig. 21b) illustrating the potential-driven kinetics of Pb deposition. It is important to note that during the potential stepping the concentration of the Pb adatoms across the graphene surface reaches its equilibrium value and further accumulation of Lead species is completely compensated by their release into the buffer solution. We believe that the accumulation limit is dependent on the concentration of the reactive sites on the graphene surface. This means that the trade-off between the nucleation rate and the quality of the Gr/SiC may be reached via controlling the defect density in graphene (defects play a role of the reactive sites). The comparison of the experimental current-time curves with theoretical ones indicates that the initial kinetics of the Pb species is governed by the three-dimensional diffusion-controlled instantaneous nucleation mechanism (Figure 21c). It was also revealed an exponential increase of the number of active nucleation sites on Gr/SiC (Fig. 21d), which is typical for an instantaneous nucleation.



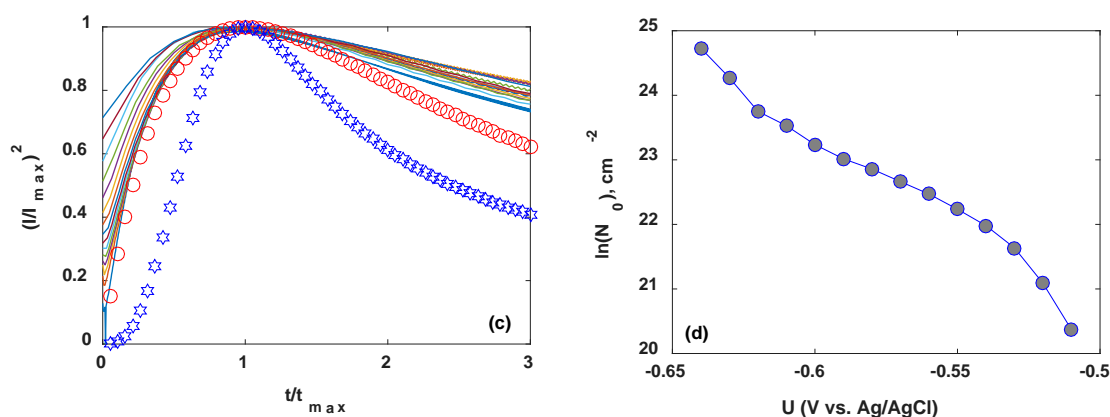


Figure 21. Dependences of the maximum current density (a) and the time corresponding to the peak current (b) on the applied deposition potential. (c) Comparison of the normalized dimensionless experimental current transient curves with theoretical ones. Blue asterisks correspond to the curve for the progressive nucleation, while the red circles represent the cases of the instantaneous nucleation. (d) $\ln(N_0)$ as a function of the applied deposition potential.

4.2. Cu kinetics

It was found that both copper reduction and oxidation reactions at the epitaxial graphene surface occur in two steps (Figure 22), which was evidenced by the presence of two reduction and two oxidation peaks. Peak R1 suggests the solid Cu formation on the epitaxial electrode surface on the negative side. The knowledge on Cu redox reactions on pristine epitaxial graphene can be considered as a starting point for further investigation of Cu kinetics, since we know the exact value of the deposition potential.

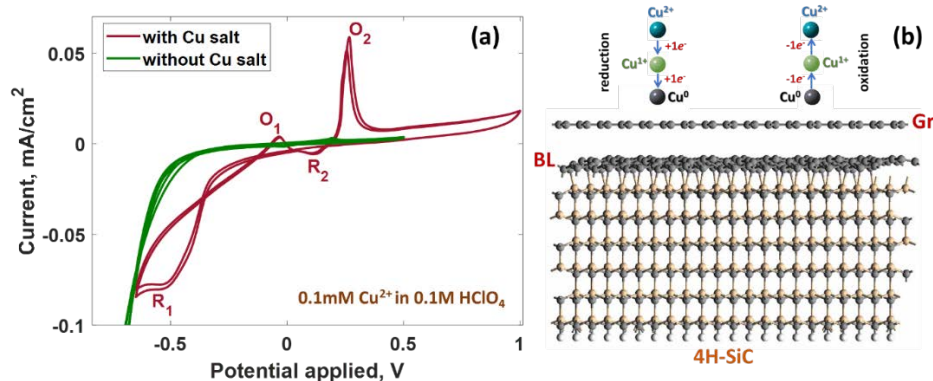


Figure 22. (a) Voltammograms related to the plating and stripping of Cu on the epitaxial graphene electrode in 0.1 M HClO₄ + 0.1 mM Cu²⁺ at $v = 20 \text{ mV}\cdot\text{s}^{-1}$ scan rate. (b) Schematic representation of the two-step Cu-involved redox reactions at the epitaxial graphene surface.

We next carried out chronoamperometry measurements and recorded current–time transients during Hg electrodeposition (Figure 23a). A comparison of the theoretical current–time curves with experimental indicates that the initial kinetics of Cu species onto the epitaxial graphene electrode is governed by the three-dimensional instantaneous growth-nucleation mechanism (Figure 23b). According to this

mechanism, the nucleation occurs on a small number density of sites and the nucleation process arrests as nucleation sites are exhausted.

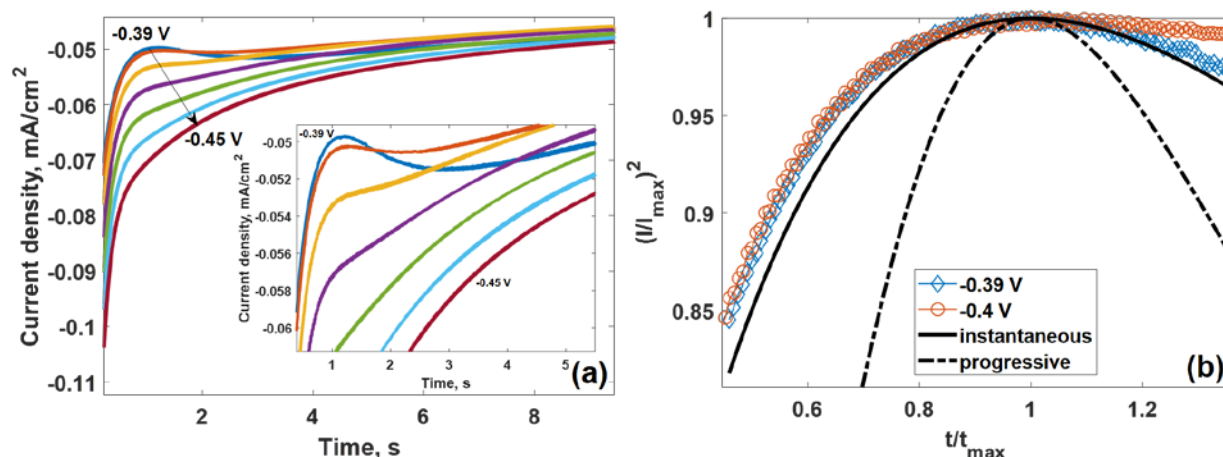


Figure 23. (a) Potentiostatic current transients for the electrodeposition of mercury onto the epitaxial graphene electrode from in 0.1 M $\text{HClO}_4 + 0.1 \text{ mM Cu}^{2+}$ recorded at the cathodic potential pulses of different amplitudes (from -0.39 V to -0.45 V). (b) Comparison of the dimensionless experimental current–time transients for the electrodeposition on mercury onto epitaxial graphene electrode with the theoretical transients for instantaneous (bold solid black curve) and progressive (bold dashed-dotted curve black curve) nucleation.

The estimated diffusion coefficient is quite small ($D=1.68 \cdot 10^{-6} \text{ cm}^2 \cdot \text{s}^{-1}$) and limits the deposition rate of metallic Cu. Whenever the electroreduced Cu species reach the graphene surface (Figure 24), they can freely diffuse across the graphene surface with small energy barrier of 35 meV (as was estimated by our DFT calculations). The presence of the second copper atom at the graphene surface significantly modifies the diffusion path due to the attractive interatomic interaction between neutral Cu species.

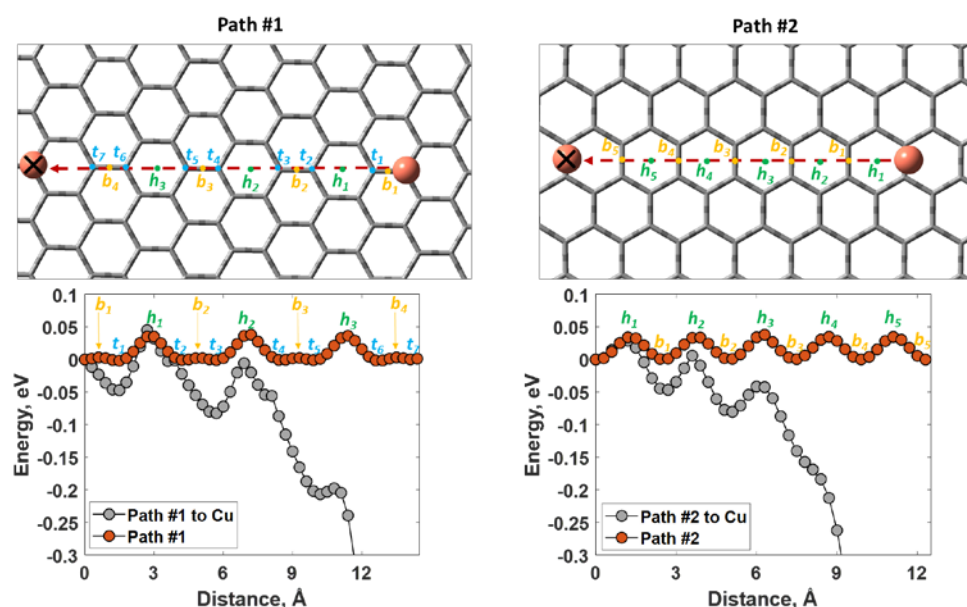


Figure 24. Possible diffusion paths for Cu on graphene and related potential energy curves.

4.3. Hg kinetics

The electrochemical redox behavior of Hg^{2+} at the epitaxial graphene working electrode is quite complicated and strongly dependent on the concentration of perchloric acid in the electrolyte solution. In 0.01 M HClO_4 buffer solution, the redox process occurs in two well-defined one-electron steps: $\text{Hg}^0 - 1e^- = \text{Hg}^{1+} - 1e^- = \text{Hg}^{2+}$, while in 0.1 M HClO_4 , mercury oxidation takes place in one two-electron step. In both cases, the anodic and cathodic peak potential separation values and current and peak area ratios indicate that the redox process is quasi-reversible. Chronoamperometry studies (Figure 25) suggest that initial kinetics of the Hg species at the Gr/SiC surface is governed by the three-dimensional instantaneous nucleation mechanism with a relatively high diffusion coefficient of $6.63 \times 10^{-2} \text{ cm}^2 \cdot \text{s}^{-1}$. Such a behavior can be attributed to the negligibly low energy barriers for surface migration of Hg across the epitaxial graphene surface and the low number density of nucleation sites at Gr/SiC ($5.59 \times 10^3 \text{ cm}^{-2}$). According to DFT calculations, the reduced Hg complex interacts with graphene mainly through weak dispersive forces, also pointing out its low binding ability and high surface migration rate at room temperature. From the point of view of sensing applications, to reach high-performance Hg detection, these parameters need to be improved. Particularly, it is necessary to increase the number of electroactive sites for Hg nucleation to enhance the interaction between Hg and epitaxial graphene.

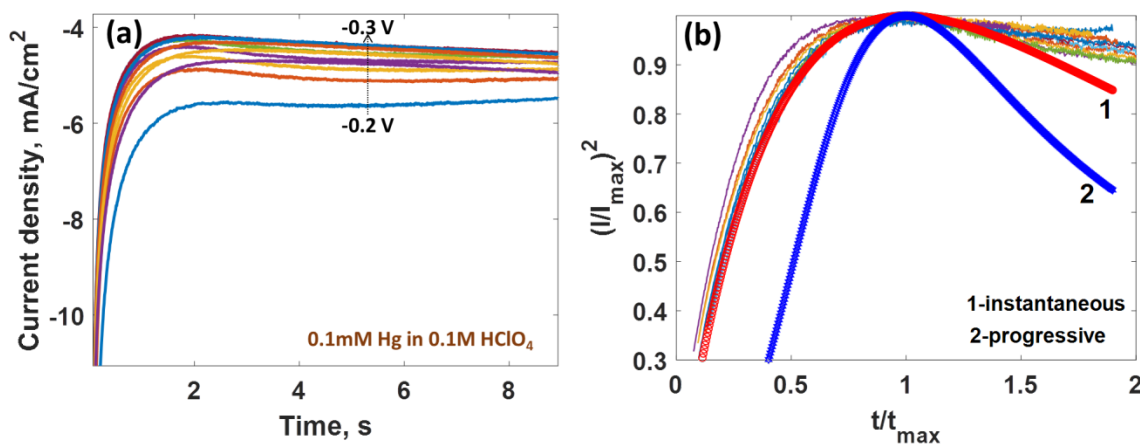


Figure 25. (a) Potentiostatic current transients for the electrodeposition of mercury onto the epitaxial graphene electrode from in 0.1 M $\text{HClO}_4 + 0.1 \text{ mM Hg}^{2+}$ recorded at the cathodic potential pulses of different amplitudes (from blue-colored curve at -0.2 V to dark red-colored curve -0.3 V). (b) Comparison of the dimensionless experimental current–time transients for the electrodeposition on mercury onto epitaxial graphene electrode with the theoretical transients for instantaneous (bold solid red curve 1) and progressive (bold solid blue curve 2) nucleation.

5. Prediction of the adsorption of heavy metals on graphene under realistic conditions

5.1. Effect of carbon vacancies

Since the formation of point defects (mostly carbon vacancies) may occur during both graphene growth process and post-growth manipulation, it is very important to understand the role of these defects in the

interaction between graphene and heavy metals (HMs). Spherically-shaped graphene nanosheets were used as a model of graphene to simulate such interaction. The vacancy engineering can promote a strong interaction between graphene and metal adsorbates, which allows for better detection of Cd, Hg and Pb. All calculated parameters are summarized in Table 1. It is obvious that the artificial creation of vacancies in graphene causes a significant increase of the binding energy of elemental heavy metals, allowing switching from a weakly physisorbed state to a strongly chemisorbed state. These changes in the interaction between metal adsorbates and graphene can be interpreted in terms of redistribution of the components contributing to the total binding energy. It was found that the monovacancy and trivacancy defects are very active for the reaction with HMs. This is due to the presence of negatively charged regions facilitating the charge transfer between metal adsorbates and graphene.

Table 1. Calculated parameters for free-standing graphene interacting with elemental heavy metals as a function of the number of removed C atoms. All calculations were performed at the PBE1PBE-D3/6-311G(d,p)/SDD level of theory.

Number of removed C atoms	Type of vacancy	Parameters					
		Binding energy, eV			Charge on HM atom		
		Cd	Hg	Pb	Cd	Hg	Pb
0	No vacancy	0.288	0.308	0.505	0.050	0.069	0.205
1	Monovacancy	1.406	2.222	5.107	0.067	0.085	0.364
2	Divacancy	0.563	0.546	3.192	0.122	0.072	0.765
3	Trivacancy	2.451	1.513	6.620	0.902	0.576	0.772
4	Tetravacancy	3.645	3.638	6.228	0.098	0.062	0.571

5.2. Substrate effect

The nature of interaction of toxic heavy metals, e.g. Cd, Hg and Pb in neutral charge state and epitaxial graphene (EG) on Si-face SiC in the absence and in the presence of pure water solution has been investigated using density functional theory with the inclusion of dispersion correction and cluster model of EG. The gas-phase calculations showed that adsorbed electro-donating Cd and Hg adatoms on EG are most stable when bonded to hollow sites, while Pb species prefer to sit above bridge sites. By using non-covalent interaction (NCI) analysis, charge decomposition analysis (CDA), overlap population density of states (OPDOS) analysis and topological analysis, it was found that the interaction between Cd or Hg and EG is non-bonding in nature and is mainly governed by van der Waals forces, while Pb adsorption is followed by the formation of anti-bonding orbitals in vacuum conditions. It was revealed that both adsorption characteristics of the heavy metals and nature of the interaction between metals and EG are strongly affected by the solvent (Table 2). In particular, water solution changed the preferred binding site of Cd and Hg adatoms from hollow site to bridge and on-top sites, respectively. The dispersion forces are expected to be the dominant factor in the interaction between EG and Cd/Hg. It was predicted that the solvent weakens the interaction energy of Pb and changes the nature of the interaction from antibonding to bonding. The obtained results give holistic understanding of the epitaxial graphene response to metals adsorption and have a significant importance because of their fundamental relevance to sensing applications, especially to electrochemical discriminative analysis of heavy metals

in drinking water. Moreover, they clearly support and explain in detail our experimental results of electrochemical sensing of Pb by epitaxial graphene, which shows much stronger signal than that of Cd and Hg.

Table 2. Parameters describing the behavior of elemental heavy metals adsorbed onto epitaxial graphene surface in the absence of water and in the presence of water. All calculations were performed at the PBE1PBE-D3/6-31G/SDD and PCM/SCRF/ PBE1PBE-D3/6-31G/SDD levels of theory.

HM	Adsorption energy, eV		Interaction energy, eV		Deformation energy, eV		Charge on atom					
	Gas	Water	Gas	Water	Gas	Water	Mulliken		Hirshfeld		ECDA	
							Gas	Water	Gas	Water	Gas	Water
Cd	0.217	0.293	0.223	0.302	0.005	0.008	0.23	0.07	-0.07	0.02	0.08	0.07
Hg	0.246	0.384	0.252	0.394	0.005	0.010	0.26	0.08	-0.01	0.03	0.15	0.08
Pb	0.641	1.57	0.827	0.533	0.185	-1.037	0.45	0.11	0.22	-0.01	0.45	0.11

5.3. Graphene thickness effect

Due to graphene thickness irregularity (according to experimental Raman data), the adsorption of heavy metal adatoms is expected on thickness-varying graphene regions (monolayer, bilayer and even trilayer). This means that the deposition/detection of metals will be determined by the different types of interactions between the metal and graphene. Therefore, the correct explanation of the experimental results requires a fundamental understanding of the adsorption mechanisms of HMs both on single-layer and multi-layer graphene. To this aim, stacked graphene nanosheets with a different number of layers (1–3) were designed as a model of graphene. The calculations predict that the number of layers does not influence the preferential adsorption sites for all considered metals (the hollow site for Cd and Hg, and the bridge site for Pb). The calculations also confirm that the second and third layer affect the binding energy of the heavy metals, though in a manner opposite to the monolayer graphene. The most important parameters describing the different adsorption configurations are summarized in Table 3. Since the charge-transfer contribution to the total interaction energy decreases for thicker graphene, it is reasonable to assume that the interlayer van-der-Waals dispersive forces (attractive in nature) between layers in graphene somehow enhance the binding energy of Cd and Hg. Unlike the adsorption of Cd and Hg, the binding energy of Pb decreases with thickness increasing, indicating the involvement of other forces in the binding mechanism. In this case, we cannot ascribe this decrease only to vanishing charge transfer term. It is obvious that the repulsive forces also contribute to the total interaction energy.

Table 3. Calculated parameters for free-standing graphene interacting with elemental heavy metals as a function of the number of graphene layers. All calculations were performed at the M06-2X/6-31G*/SDD level of theory.

Number of Graphene layers	Parameters					
	Binding energy, eV			Charge on HM atom		
	Cd	Hg	Pb	Cd	Hg	Pb
1	0.410	0.4049	0.5383	0.106	0.133	0.314
2	0.422	0.4109	0.5208	0.096	0.122	0.267
3	0.429	0.4328	0.5288	0.094	0.119	0.238

Dissemination of project results

Papers published in peer-reviewed journals (with acknowledgments to The ÅForsk foundation)

1. **Shteplyuk, I.**, Eriksson, J., Khranovskyy, V., Iakimov, T., Spetz, A.L., Yakimova, R.
Monolayer graphene/SiC Schottky barrier diodes with improved barrier height uniformity as a sensing platform for the detection of heavy metals (2016) *Beilstein Journal of Nanotechnology*, 7, pp. 1800-1814. Cited 14 times.
DOI: 10.3762/bjnano.7.173
2. **Shteplyuk, I.**, Khranovskyy, V., Yakimova, R.
Combining graphene with silicon carbide: Synthesis and properties - A review. (2016) *Semiconductor Science and Technology*, 31 (11), art. no. 113004, . Cited 13 times.
DOI: 10.1088/0268-1242/31/11/113004
3. **Shteplyuk, I.**, Caffrey, N.M., Iakimov, T., Khranovskyy, V., Abrikosov, I.A., Yakimova, R.
On the interaction of toxic Heavy Metals (Cd, Hg, Pb) with graphene quantum dots and infinite Graphene (2017) *Scientific Reports*, 7 (1), art. no. 3934. Cited 30 times.
DOI: 10.1038/s41598-017-04339-8
4. **Shteplyuk, I.**, Khranovskyy, V., Yakimova, R.
Insights into the origin of the excited transitions in graphene quantum dots interacting with heavy metals in different media (2017) *Physical Chemistry Chemical Physics*, 19 (45), pp. 30445-30463. Cited 12 times.
DOI: 10.1039/c7cp04711h
5. **Shteplyuk, I.**, Iakimov, T., Khranovskyy, V., Eriksson, J., Giannazzo, F., Yakimova, R. Role of the potential barrier in the electrical performance of the graphene/SiC interface (2017) *Crystals*, 7 (6), art. no. 162. Cited 11 times.
DOI: 10.3390/cryst7060162
6. Tencha, A., Fedoriv, V., **Shteplyuk, I.**, Yakimova, R., Ivanov, I., Khranovskyy, V., Shavanova, K., Ruban, Y.
Synthesis of graphene oxide inks for printed electronics (2017) *2017 IEEE International Young Scientists Forum on Applied Physics and Engineering, YSF 2017*, 2017-January, pp. 155-158. Cited 1 time.
DOI: 10.1109/YSF.2017.8126608
7. **Shteplyuk, I.**, Vagin, M., Ivanov, I.G., Iakimov, T., Yazdi, G.R., Yakimova, R.
Lead (Pb) interfacing with epitaxial graphene (2018) *Physical Chemistry Chemical Physics*, 20 (25), pp. 17105-17116. Cited 6 times.
DOI: 10.1039/c8cp01814f
8. **Shteplyuk, I.**, Yakimova, R.

Interband absorption in few-layer graphene quantum dots: Effect of heavy metals (2018) *Materials*, 11 (7), art. no. 1217. Cited 5 times.

DOI: 10.3390/ma11071217

9. **Shtepliuk, I.**, Yakimova, R.

Interband transitions in closed-shell vacancy containing graphene quantum dots complexed with heavy metals (2018) *Physical Chemistry Chemical Physics*, 20 (33), pp. 21528-21543. Cited 5 times.

DOI: 10.1039/c8cp03306d

10. **Shtepliuk, I.**, Santangelo, M.F., Vagin, M., Ivanov, I.G., Khranovskyy, V., Iakimov, T., Eriksson, J., Yakimova, R.

Understanding graphene response to neutral and charged lead species: Theory and experiment (2018) *Materials*, 11 (10), art. no. 2059. Cited 4 times.

DOI: 10.3390/ma11102059

11. Khranovskyy, V., **Shtepliuk, I.**, Vines, L., Yakimova, R.

Complementary study of the photoluminescence and electrical properties of ZnO films grown on 4H-SiC substrates (2017) *Journal of Luminescence*, 181, pp. 374-381. Cited 4 times.

DOI: 10.1016/j.jlumin.2016.09.042

12. **Santangelo, M.F.**, Shtepliuk, I., Filippini, D., Ivanov, I.G., Yakimova, R., Eriksson, J.

Real-time sensing of lead with epitaxial graphene-integrated microfluidic devices (2019) *Sensors and Actuators, B: Chemical*, 288, pp. 425-431. Cited 3 times.

DOI: 10.1016/j.snb.2019.03.021

13. **Shtepliuk, I.**, Ivanov, I.G., Iakimov, T., Yakimova, R., Kakanakova-Georgieva, A., Fiorenza, P., Giannazzo, F.

Raman probing of hydrogen-intercalated graphene on Si-face 4H-SiC (2019) *Materials Science in Semiconductor Processing*, 96, pp. 145-152. Cited 2 times.

DOI: 10.1016/j.mssp.2019.02.039

14. Rodner, M., Puglisi, D., Ekeröth, S., Helmersson, U., **Shtepliuk, I.**, Yakimova, R., Skallberg, A., Uvdal, K., Schütze, A., Eriksson, J.

Graphene decorated with iron oxide nanoparticles for highly sensitive interaction with volatile organic compounds (2019) *Sensors (Switzerland)*, 19 (4), art. no. 918. Cited 2 times.

DOI: 10.3390/s19040918

15. Yazdi, G.R., Akhtar, F., Ivanov, I.G., Schmidt, S., **Shtepliuk, I.**, Zakharov, A., Iakimov, T., Yakimova, R.

Effect of epitaxial graphene morphology on adsorption of ambient species (2019) *Applied Surface Science*, 486, pp. 239-248. Cited 1 time.

DOI: 10.1016/j.apsusc.2019.04.247

16. Giannazzo, F., **Shtepliuk, I.**, Ivanov, I.G., Iakimov, T., Kakanakova-Georgieva, A., Schiliro, E., Fiorenza, P., Yakimova, R.

Probing the uniformity of hydrogen intercalation in quasi-free-standing epitaxial graphene on SiC by micro-Raman mapping and conductive atomic force microscopy (2019) *Nanotechnology*, 30 (28), art. no. 284003. Cited 1 time.

DOI: 10.1088/1361-6528/ab134e

17. Santangelo, M.F., **Shtepliuk, I.**, Filippini, D., Puglisi, D., Vagin, M., Yakimova, R., Eriksson, J. Epitaxial graphene sensors combined with 3D-printed microfluidic chip for heavy metals detection (2019) *Sensors (Switzerland)*, 19 (10), art. no. 2393.

DOI: 10.3390/s19102393

18. **Shtepliuk, I.**, Vagin, M., Iakimov, T., Yakimova, R.

Fundamentals of environmental monitoring of heavy metals using graphene (2019) *Chemical Engineering Transactions*, 73, pp. 7-12.

DOI: 10.3303/CET1973002

19. **Shtepliuk, I.**, Yakimova, R.

Interaction of epitaxial graphene with heavy metals: Towards novel sensing platform (2019) *Nanotechnology*, 30 (29), art. no. 294002.

DOI: 10.1088/1361-6528/ab1546

20. **Shtepliuk, I.**; Vagin, M.; Yakimova, R.

Insights into the Electrochemical Behavior of Mercury on Graphene/SiC Electrodes. (2019) *C - Journal of Carbon Research*, 5, 51, pp. 1-14.

DOI:10.3390/c5030051

21. **Shtepliuk, I.**, Ivanov, I.G., Vagin, M., Khan, Z., Iakimov, T., Pliatsikas, N., Sarakinos, K., Giannazzo, F., and Yakimova, R.

Manipulation of epitaxial graphene towards novel properties and applications, (2019) *Materials Today: Proceedings*, in press.

DOI: 10.1016/j.matpr.2019.08.213

22. **Shtepliuk, I.**, Ivanov, I. G., Pliatsikas, N., Iakimov, T., Jamnig, A., Sarakinos, K., Yakimova, R.

Probing the uniformity of silver-doped epitaxial graphene by micro-Raman mapping, (2019) *Physical B: Condensed Matter*, in press.

DOI: 10.1016/j.physb.2019.411751

Popular science articles

1. V. Khranovskyy, R. Yakimova, **I. Shtepliuk**, P. Lima de Carvalho, and A. Pinto, Energy saving filter for removal of heavy metals from water, (2017) *Tech Briefs*, 41, №11, p. 30.

2. V. Khranovskyy, **I. Shtepliuk**, R. Yakimova, Addressing environmental threats, (2018) *SciTech Europa*, Quarterly 26, 1-2

Oral presentations at conferences and symposia

1. **I. Shtepliuk**, J. Eriksson, V.Khranovskyy, T. Iakimov, A.L. Spetz, and R. Yakimova, Monolayer graphene/SiC Schottky barrier diodes with improved barrier height uniformity as a sensing platform for

detection of heavy metals// AFM 2016 conference, Norrköping, Kolmården Sweden, from 22-24 August, 2016.

2. **Ivan Shtepliuk**, Volodymyr Khranovskyy, Jens Eriksson, Anita L. Spetz, Rositsa Yakimova, Detection of heavy metals using epitaxial graphene on SiC, EMRS Spring Meeting 2016, Lille (France) from May 2 to 6.

3. **Ivan Shtepliuk**, Mikhail Vagin, Marius Rodner, Jens Eriksson, Tihomir Iakimov, Volodymyr Khranovskyy, Anita Lloyd Spetz and Rositsa Yakimova, Graphene/SiC platform towards Lead detection in aqueous solutions, Graphene-2017, March 28-31, Barcelona, Spain.

4. R. Yakimova, **I. Shtepliuk**, M. Vagin, T. Iakimov, J. Eriksson, Towards versatile sensing platform based on graphene, Twentieth International Summer School VEIT-2017, 25 - 29 September 2017, Sozopol, Bulgaria.

5. **I. Shtepliuk**, M. Vagin, V. Khranovskyy, T. Iakimov, R. Yakimova, Theoretical and experimental insights into detection of toxic heavy metals by epitaxial graphene on SiC, International Symposium on Epitaxial Graphene 2017, 22-25 November 2017, Nagoya University, Japan.

6. **I. Shtepliuk**, M. Vagin, I.G. Ivanov, T. Iakimov, R. Yazdi, V. Khranovskyy and R. Yakimova, Theoretical and experimental insights into detection of toxic heavy metals by graphene-based materials Minisymposium “Nanomaterials for Sensors and Energy Applications”, November 1-2, 2017, Vadstena Klosterhotell, Vadstena, Sweden.

7. R. Yakimova, **I. Shtepliuk**, M. Vagin, I.G. Ivanov, T. Iakimov, G.R. Yazdi, J. Eriksson, Epitaxial Graphene on SiC - Status and Prospects, CIMTEC 2018, 8th Forum on New Materials, June 10-14/2018, Perugia, Italy.

8. **I. Shtepliuk**, M. Vagin, I. Ivanov, T. Iakimov, R. Yakimova, Understanding the Kinetics of Heavy Metals on Epitaxial Graphene: Towards Monitoring the Water Quality, CIMTEC 2018, 8th Forum on New Materials, June 10-14/2018, Perugia, Italy.

9. R. Yakimova, **I. Shtepliuk**, M. Vagin, J. Eriksson, Towards sensing platform based on epitaxial graphene, 14th International Conference on Diffusion in Solids and Liquids, 25-29 June, 2018 Amsterdam, The Netherlands.

10. R. Yakimova, **I. Shtepliuk**, M. Francesca Santangelo, M. Vagin, T. Iakimov and J. Eriksson, Interaction of epitaxial graphene with heavy metals: towards novel sensing platform, International Conference Tunneling Through Nanoscience, TTN-2018 International Conference, October 17 - 20, 2018 Ravello, Italy.

11. R. Yakimova, **I. Shtepliuk**, M. Francesca Santangelo, M. Vagin, T. Iakimov and J. Eriksson, Insights into detection of toxic metals by Graphene: theory and experiment, The 6th International Symposium on Graphene Devices (ISGD-6), 18-21 July, 2018, St. Petersburg, Russia.

12. **I. Shtepliuk**, M.F. Santangelo, M. Vagin, I. G. Ivanov, J. Eriksson, R. Yakimova, Fundamentals of environmental monitoring of heavy metals using graphene, Abstracts of 3rd International Conference on Nanotechnology based Innovative Applications for the environment, 14-17 April 2019, Naples, Italy.

13. **I. Shtepliuk**, M. Vagin, Z. Khan, I.G. Ivanov, T. Iakimov, R. Yakimova, Electrochemical lithiation of epitaxial graphene for rechargeable batteries, p.100. Abstracts of Nano-M&D 2019 “Fabrication, Properties, and Applications of Nano-Materials and Nano-Devices”, June 04-08, 2019, Savoy Beach Hotel, Paestum, Salerno (Italy).
14. **I. Shtepliuk**, I. G. Ivanov, T. Iakimov, A. Jamnig, B. Pecz, F. Giannazzo, R. Yakimova, K. Sarakinos, Effect of thin silver films on vibrational properties of epitaxial graphene, Symp. N: Nano-engineered coatings and thin films: from design to applications, May 27 to 31, 2019, Nice (France).
15. **I. Shtepliuk**, M. Vagin, Z. Khan, I. G. Ivanov, T. Iakimov, B. Pecz, F. Giannazzo, K. Sarakinos, R. Yakimova, Interplay of metals and epitaxial graphene on SiC, Symp. X: Silicon carbide and related materials for energy saving applications, May 27 to 31, 2019, Nice (France).